Title

Graphene sensing meshes for densely distributed strain field monitoring

Journal

Structural Health Monitoring, 19(5)

ISSN

1475-9217

Authors

Gupta, Sumit
Vella, Gianmarco
Yu, I-No
et al.

Publication Date

2020-09-01

DOI

10.1177/1475921719877418

Peer reviewed

Graphene Sensing Meshes for Densely Distributed Strain Field Monitoring

Sumit Gupta[1], Gianmarco Vella[2*], I-No Yu[3], Chin-Hsiung Loh[1,3], Wei-Hung Chiang[4], and Kenneth J. Loh[1,2]

[1] *Department of Structural Engineering, University of California-San Diego, La Jolla, CA 92093-0085, USA*
[2] *Material Science and Engineering Program, University of California-San Diego, La Jolla, CA 92093, USA*
[3] *Department of Civil Engineering, National Taiwan University, Taipei 10617, Taiwan*
[4] *Department of Chemical Engineering, National Taiwan University of Science & Technology, Taipei 10617, Taiwan*
[*] *Corresponding author e-mail:* kenloh@ucsd.edu

Abstract

The objective of this study is to design and validate distributed strain field monitoring using a patterned nanocomposite "sensing mesh" coupled with an electrical impedance tomography (EIT) measurement strategy and algorithm. Although EIT has been used in other studies and in conjunction with a piezoresistive thin film for spatial damage detection, different strain components cannot be directly extracted from reconstructed EIT conductivity maps. Therefore, this study seeks to address this issue by patterning piezoresistive graphene-based thin films to form a mesh-like pattern. The high aspect ratio of each nanocomposite grid interconnect acts as a linear distributed strain sensor, capable of resolving strains along the entire length and direction of the element. This study first began with the design, fabrication, and characterization of the strain sensing response of a graphene-based thin film of high strain sensitivity. Second, the strain-sensitive film was spray-coated onto patterned polymer substrates to form the sensing meshes, which were then subjected to load tests. Upon validating distributed strain field monitoring through EIT, its applicability for field implementation and damage characterization was also demonstrated by instrumenting sensing meshes in the column of a seven-story reinforced-concrete building subjected to shaking table earthquake excitations. The large-scale shaking table test results successfully validated distributed damage detection.

Keywords: Electrical impedance tomography, graphene, large-scale testing, nanocomposite, patterning, spray coating, strain field, strain sensing, structural health monitoring, thin film.

I. Introduction

The performance of civil structures (*e.g.*, buildings, bridges, and pipelines, among others) often deteriorates over time, especially if they are subjected to extreme events and harsh operating conditions. In addition, many structures experience repetitive dynamic loads that can induce fatigue and local material failure. For example, bowing and cracking in steel, as well as various types of crushing and cracking in concrete, are typical damage modes for civil structures. These damage precursors can grow to form defects, flaws, and damage at an early stage, which can then propagate if left unmitigated to potentially cause catastrophic failure. Hence, condition monitoring is important for critical engineered structures and is necessary to ensure their safety, reliability, and functionality over time.

Structural health monitoring (SHM), which is performed either periodically or in a continuous manner, aims to provide timely and accurate information about the presence, severity, and location of damage for better decision making and maintenance.[1] Among the various parameters, stress is of great interest in SHM since system or material failures are often defined by stress-related limit states (*e.g.*, yield stress or the ultimate tensile strength). Unfortunately, stress is an engineered quantity and cannot be directly measured, but it may be evaluated using known or assumed stress-strain relations. Thus, strain is an important parameter that is often directly measured for SHM. Furthermore, anomalies in strain distributions can indicate the presence of damage as highly localized strain is indicative of cracking or local buckling.

One of the most widely used strain measuring instruments is a foil-based strain gage that is directly attached to the structural surface of interest. Despite their low cost, high accuracy, and high resolution, they are discrete sensors that need to be densely instrumented for quantifying the strain distribution of a structural component. On the other hand, fiber Bragg grating (FBG) sensors offer several advantages versus other electronic-based strain transducers (*e.g.*, fast response, resistance to corrosion, and immunity to electromagnetic noise and radio frequency interference).[2] The ability to multiplex and measure strains at different locations is another major advantage. However, complex and expensive equipment is often needed to interrogate FBGs, and their high manufacturing and installation costs are impediments to practical use.[3]

As a result, these limitations have spurred the development of other types of strain sensors derived from different sensing mechanisms. For example, Glisic *et al.*[4] studied large-area electronics and crystalline silicon complementary metal-oxide-semiconductor integrated-circuit-based strain sensors for large-scale structural sensing applications. Kharroub *et al.*[5] developed soft elastomeric capacitor-based thin film sensors for detecting and localizing fatigue-induced cracks in steel structures.

More recently, another approach is to design and tune materials to enable them with desired sensing functionalities. For instance, material-based strain sensors are designed such that their electrical properties (*e.g.*, conductivity) respond to strain and deformation. In particular, with the advent of nanotechnology and the availability of a wide variety of nanomaterials, various types of strain sensors have been successfully demonstrated. A carbon nanotube (CNT) buckypaper with linear strain sensing behavior was explored by Dharap *et al.*[6] Shortly thereafter, Loh *et al.*[7] infused CNTs into a polymer matrix, using layer-by-layer (LbL) self-assembly, to develop a strain sensor with a broader sensing range and improved mechanical properties.

However, to fully take advantage of the fact that these materials and nanocomposites are sensitive to some stimulus at every location in the material, it was shown that spatial sensing could be achieved using an electrical impedance tomography (EIT) measurement technique and algorithm. In fact, EIT was first successfully used by Hou *et al.*[8] for mapping the conductivity distribution of a multifunctional CNT thin film for sensing and localizing physical, chemical, and mechanical changes. LbL CNT-polymer thin films, also referred to as "sensing skins", were also coupled with EIT for validating spatial strain monitoring and damage detection in an aluminum plate subjected to low-energy impact[9]. Later, Loyola *et al.*[10] was able to embed strain-sensitive CNT-based thin films in glass fiber-reinforced polymer (GFRP) composites to quantify nonvisible and subsurface impact damage. EIT was also applied by Hallaji *et al.*[11] for surface crack and damage detection in a concrete beam through the use of a conductive silver paint coating. More recently, Gupta *et al.*[12] showed that CNT-polymer thin films could be used to modify the interfacial transition zones in concrete to design multifunctional self-sensing structural materials.

Piezoresistive sensing skins coupled with the EIT algorithm opened up vast opportunities for distributed strain sensing. However, two main drawbacks persist. First, a separate analytical inverse piezoresistive numerical model is required to extract strain directionality from the reconstructed EIT conductivity maps.[13] Second, comparatively low strain sensitivities of the CNT thin films make it challenging for detecting small changes in strain.

To address these limitations, this study introduces a new "sensing mesh" concept. First, a graphene-based thin film of high strain sensitivity was designed and fabricated. The nanocomposite films were deposited onto laser-cut patterned polyethylene terephthalate (PET) substrates by means of spray coating to form the sensing meshes. Each strut of the sensing mesh was designed to have a high aspect ratio, thereby forming an interconnected equivalent network of uniaxial linear distributed strain sensors. Second, an EIT algorithm was implemented for reconstructing the spatial conductivity distribution of the sensing mesh.

This paper begins with the mathematical background of EIT, followed by a discussion of the sensing mesh fabrication procedure and experiments. Upon confirming the enhanced strain sensing response of the graphene-based films, the sensing mesh was experimentally validated to measure distributed strain fields. As further validation, the sensing mesh was also employed to measure spatial strain distribution of different structural surfaces subjected to different levels of tensile loading. Finally, the sensing mesh was demonstrated for its ability to monitor different damage states in a seven-story reinforced-concrete (RC) structure subjected to shaking table tests.

II. EIT Background

EIT is a soft-field imaging technique where the electrical conductivity distribution of a conductive body is reconstructed from a limited number of boundary voltage measurements.[14, 15] Since the 1980s, EIT has been successfully used in the biomedical domain for detecting anomalies inside the human body through reconstructed

conductivity maps.[16-20] More recently, EIT has been adopted for applications in SHM.[21] In general, electrodes are arranged along the perimeter of the conductive object. A direct current (DC) is applied to a pair of boundary electrodes, while the voltage drops are recorded at all remaining boundary electrodes. This excitation-measurement pattern is repeated for all boundary electrodes. An inverse problem is then solved based on this input-output relationship to reconstruct the conductivity distribution of the conductive body.

In essence, EIT consists of the forward and inverse problems. The forward problem is employed to estimate the electrical voltage distribution at the boundary electrodes, while the electrical excitation and conductivity distribution are known *a priori*. However, for experimental implementations, the EIT inverse problem needs to be solved for reconstructing spatial conductivity from the measured set of boundary voltage responses. Both the EIT forward and inverse problems are briefly discussed in the following sections.

A. EIT Forward Problem

As mentioned earlier, the EIT forward problem is solved to estimate the boundary voltage distribution of a conductive body (Ω) with an explicitly known electrical conductivity distribution (σ). Mathematically, the EIT forward problem can be described by 2D Laplace's equation as shown in (1):

$$\nabla \cdot (\sigma \nabla u) = 0 \tag{1}$$

where u is the electrical potential distribution in Ω. In general, a finite element model (FEM) is used to solve (1) with boundary conditions known as the complete electrode model.[14, 15] In many cases, Ω is modeled as a simple 2D plate and discretized using linear triangular[10, 14, 15] or bi-linear quadrilateral elements.[12]

In this study, the sensing meshes are not continuous thin films but rather patterned grid-like piezoresistive networks. Because of the high aspect ratio of each "strut" in the sensing mesh, induced strains in each strut are confined along their longitudinal axes, experiencing either uniaxial tensile or compressive strains. This is analogous to the axial elements that make up a truss structure. Therefore, this same idea is adopted to capture the uniaxial changes in conductivity of each strut in the sensing mesh. However, this also requires a different FEM implementation for EIT spatial conductivity mapping. Here, the high aspect ratio of each strut and the entire sensing mesh was modeled as a 2D truss structure discretized using 1D linear bar elements. By doing so, the computational cost to solve the forward problem, as well and the sensitivity matrix (J), was significantly reduced. A reduction in the size of the sensitivity matrix eases its inversion during the execution of the inverse problem. In addition, a point electrode model[22] was implemented; the specified boundary conditions are shown in (2) below:

$$\sigma \frac{\partial u}{\partial n} = f \text{ on } \Gamma$$
$$f = \sum_{i=1}^{M} I \delta_{x_i} \tag{2}$$

where I is the magnitude of current injected into Ω during EIT interrogation, Γ is the boundary of Ω, M is the number of boundary electrodes, n is the outward unit normal at the boundary, and δ_{x_i} is the Dirac-Delta function on Γ supported at x_i. An essential boundary condition (*i.e.*, $u = 0$) should also be imposed on the electrode that is grounded during electrical excitation. A weak form of (1) was derived by multiplying it with a sufficiently smooth test function (φ) and integrating over Ω as shown in (3):

$$\int_{\Omega} \sigma \nabla u \cdot \nabla \varphi d\Omega = \int_{\Gamma} f \varphi d\Gamma \tag{3}$$

Then, a set of linear equations obtained from (3) are solved to obtain u at each node of the discretized Ω.

B. Inverse Problem

The EIT inverse problem aims to reconstruct the conductivity distribution using an experimentally measured set of boundary voltage responses. A single-step linear inverse solver with Tikhonov regularization was used to estimate the conductivity change ($\Delta\sigma$) from the observed change in boundary voltage distribution (ΔV) between two states,

$$\Delta\sigma = \left(J^T J + \alpha^2 I\right)^{-1} J^T \Delta V \tag{4}$$

where α is the regularization parameter, and I is the identity matrix.[23] Here, the sensitivity method was adopted to compute J.[24] Each term of J (*i.e.*, J_{lkn}), which is the derivative of the measured boundary voltage with respect to the conductivity of each finite element voxel, is evaluated using (5):

$$J_{lkn} = \frac{\partial U_l^k}{\partial \sigma_n} = \int_{L_n} \nabla u_l \cdot \nabla u_k dl \tag{5}$$

where u_l and u_k are the voltage distributions when the l^{th} and k^{th} current patterns are used, respectively. L_n is the length of the n^{th} finite element, σ_n is the conductivity of the n^{th} finite element, and U_l^k is the k^{th} measured boundary voltage when the l^{th} excitation pattern is used. More details of the EIT theory and implementation can be found in other studies.[12, 14, 15]

III. Experimental Details

A. Nanocomposite thin film preparation

In order to achieve distributed strain field monitoring, the first step was to design and fabricate a nanocomposite thin film whose electrical conductivity (or resistivity) was sensitive to applied strains and deformation. Among the variety of nanomaterials that are available today, a significant body of current research focuses on graphene nanosheets (GNS), which exhibits outstanding intrinsic properties, with piezoresistivity being just one of them. For example, Chen *et al.*[25] demonstrated that the Young's modulus of single-layer graphene sheet could be as high as 1 TPa with a gage factor of 11.4. Several studies already showed that GNS could be integrated into polymer matrices to form high-performance strain sensors.[26-29]

The GNS that was used in this work was synthesized using water-assisted liquid-phase exfoliation. The synthesis procedure was explained in detail in Manna *et al.*[30, 31] but is also summarized here for completeness. The process began by mixing microcrystalline graphite powder with an aqueous solution of N-methyl-2-pyrrolidone (NMP), followed by 6 h of bath sonication at a fixed nominal power (100 W) and frequency (37 kHz). Thereafter, the sonicated graphene-NMP solution was centrifuged at 3,000 rpm for 30 min. The upper 75% of the centrifuged colloidal solution (*i.e.*, the supernatant) was collected and then dried to obtain agglomerated GNS. The GNS-based thin film strain sensor was then fabricated by dispersing them in a poly(vinyl alcohol) (PVA) polyelectrolyte solution. The GNS-PVA ink fabrication process is discussed in the next two sub-sections.

A.1. PVA solution preparation

GNS, which is hydrophobic, requires a hydrophilic group to facilitate dispersion. Steric stabilization of GNS in PVA (Sigma-Aldrich), which is hydrophilic in nature, not only disperses GNS in the solution but also allows them to adsorb onto various substrates and form thin films. The PVA used in this work is amorphous and has a molecular weight of 146,000 – 186,000 g/mol and a hydrolysis degree of ~ 99%+. Preparation of the 5 *wt.*%. PVA solution began by boiling 95 mL of deionized (DI) water using a hot plate while continuously stirring the solution using a magnetic stirrer operated at 300 rpm. Then, 5 g of PVA powder was slowly added to the boiling DI water. The mixture was stirred until a visibly clear and fully dissolved PVA solution was obtained. The final step was to cool the PVA solution to room temperature.

A.2. GNS-PVA ink preparation

The aforementioned 5 *wt.*% PVA solution was directly used to prepare the GNS-PVA ink. While various methods could be used to disperse GNS in aqueous media, ultrasonication was employed due to its simplicity and effectiveness. In short, ultrasonication of fluidic solutions, such as GNS in PVA, by creating cavitation.[32] Cavitation forms relatively low-pressure zones and creates bubbles. Bubbles formed at the surface of solid particles (*i.e.*, on the GNS) rapidly expand, causing the solid particles to break apart and separate from each other. The size of the bubble produced during cavitation is governed by the frequency of the ultrasound, where higher frequencies produce smaller bubbles.[32]

In this study, a 1 *wt.*% GNS-PVA mixture was prepared by subjecting it to high-energy probe sonication (150 W, 22 kHz, and running a 5-s-on/5-s-off sonication cycle) for 1 h. The dispersed GNS-PVA ink was then used as is and directly spray-coated onto PET substrates using a Paasche airbrush operated at a constant air pressure of ~ 10 psi to

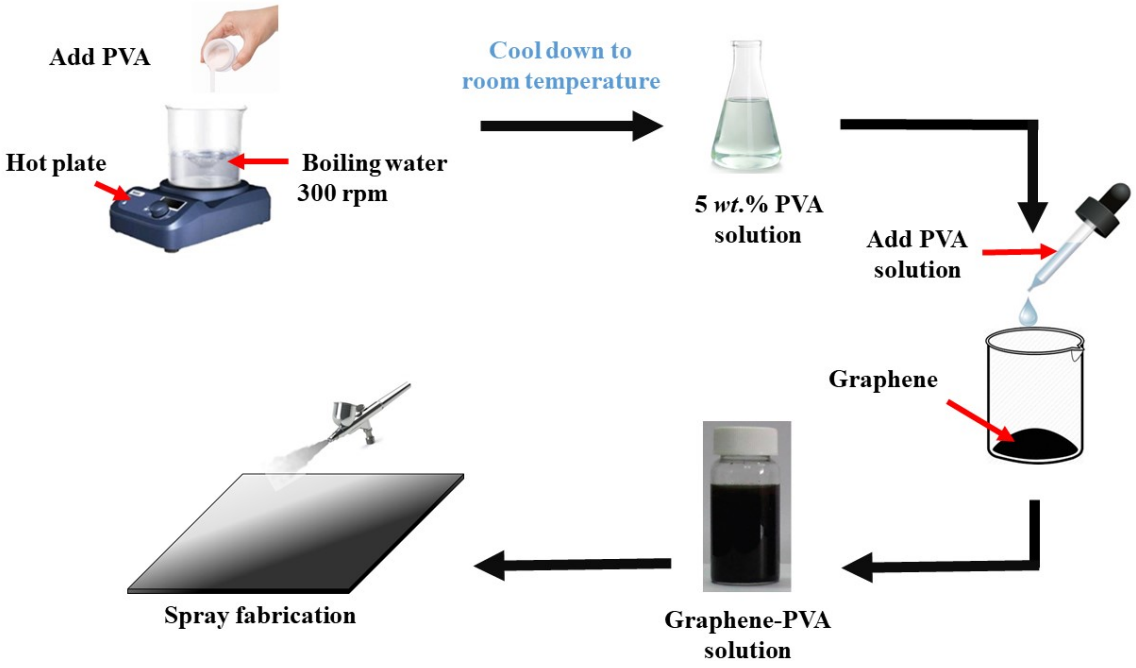

Figure 1. The GNS-PVA ink preparation and spray fabrication process are illustrated.

avoid droplet scattering in the air and splashing on the substrate. Spray fabrication was performed manually by holding the airbrush ~ 15 cm above the substrates. After depositing a uniform layer of thin film on the PET substrate, they were kept inside the fume hood and allowed to completely dry. Thereafter, airbrushing was repeated. This spraying and drying cycle was repeated three times to obtain a consistent and uniform thin film on the PET grid. The entire GNS-PVA thin film fabrication process is illustrated in Fig. 1.

Spray fabrication was adopted in this study because one could produce high-quality and large-scale GNS-PVA thin films quickly. In a previous study by Loh *et al.*[9], a CNT-based thin film strain sensor was fabricated by means of LbL. LbL required more than a day to fabricate a 20 × 10 mm^2 thin films. In contrast, spray fabrication can deposit homogeneous thin films within minutes. Although a manual procedure was employed in this work, spraying can be fully automated through the use of robotic spray systems. Furthermore, spraying is beneficial as one can directly deposit films onto various (and masked) structural surfaces, thereby eliminating problems associated with gluing sensing meshes and issues regarding nonuniform strain transfer from the structural surface to the sensing element.

B. Strain Sensing Characterization

The strain sensing performance of the GNS-PVA thin films that were deposited onto PET substrates was characterized by subjecting them to uniaxial tensile cyclic strains, while their electrical responses were simultaneously measured. First, the air-dried thin film specimens were cut to form thin rectangular strips (60 mm × 10 mm) and instrumented with two electrodes at its opposite ends, as is shown in Fig. 2. Conductive threads (Adafruit) were used as electrodes and attached to the films using conductive colloidal silver paint (Ted Pella). A total of four specimens were prepared and tested.

The GNS-PVA thin film strips were mounted in a Test Resources 150R load frame with a 1.1 lbf (4.9 N) load cell as shown in Fig. 2. Upon ensuring that the thin film was taut, the load frame was programmed to execute a three-cycle tensile cyclic strain pattern to a maximum of 5,000 με at a constant strain rate of 15,000 με/min. A Keysight 34465A digital multimeter (DMM) was used throughout testing to measure thin film resistance. *BenchVue* data logging software was used to record all the measurements at a sampling rate of 2 Hz.

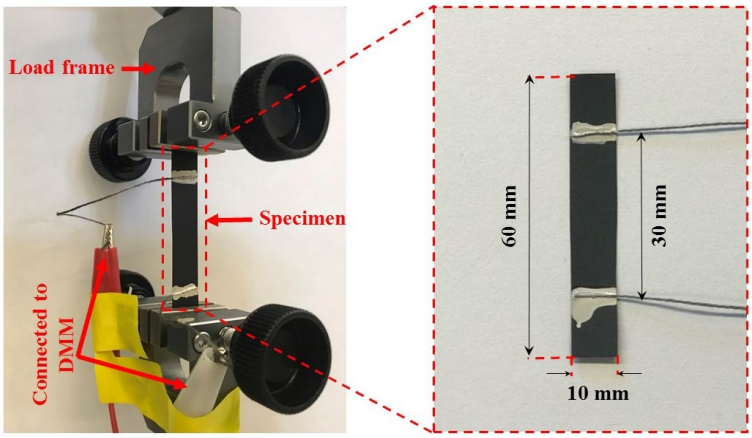

Figure 2. GNS-PVA thin films were deposited onto PET rectangular strip substrates. These rectangular specimens were instrumented with two electrodes for electrical measurements and then mounted in a load frame for strain sensing characterization tests.

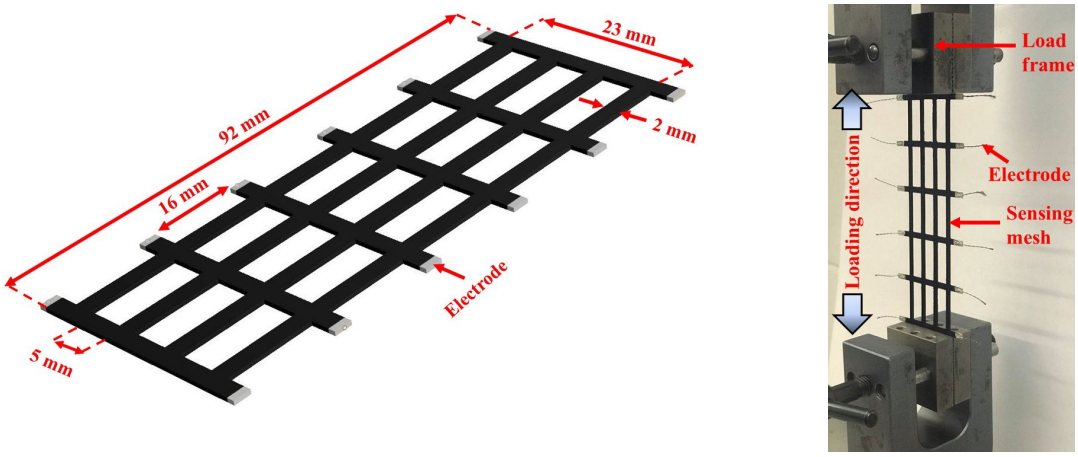

(a) (b)

Figure 3. (a) PET sheets were cut into grid-like patterns using a laser cutter, followed by spray-coating them with GNS-PVA ink to form the sensing mesh specimens. (b) The sensing mesh was mounted in a load frame and subjected to uniaxial tensile loading. EIT measurements were acquired at different strain states, while the load frame was paused.

C. Sensing Mesh Validation

As was mentioned earlier, GNS-PVA thin films were deposited onto PET grids to form sensing mesh specimens. The patterns were first sketched in *AutoCAD* and then exported to *LaserDRW*. A 40 W CO_2 laser cutter (Orion Motor Tech) was used for patterning the PET grids. Three sets of sensing mesh tests were conducted.

First, the sensing mesh was instrumented with 12 boundary electrodes (Fig. 3a) for EIT interrogation and loaded in the Test Resources 150R load frame for spatial strain sensing characterization, as is shown in Fig. 3b. It should be observed from Fig. 3 that the sensing mesh consisted of only horizontal and vertical struts. The load frame was programmed to stretch the sensing mesh from 0 to 5,000 με at a constant rate of 15,000 με/min. An initial baseline measurement was recorded prior to applying any load. At every 1,000 με increments, the load frame was manually paused, and EIT measurements were collected. A Keithley 6221 current generator was interfaced with a Keysight 34980A multifunctional switch for interrogating the sensing mesh. A custom *MATLAB* software was employed to control the Keysight switch and its built-in DMM for acquiring boundary voltage measurements during EIT testing. Current injection and boundary voltage measurements followed the adjacent electrode model as was done in previous studies.[10] Boundary voltage measurements were then used as inputs to the EIT inverse problem for reconstructing the

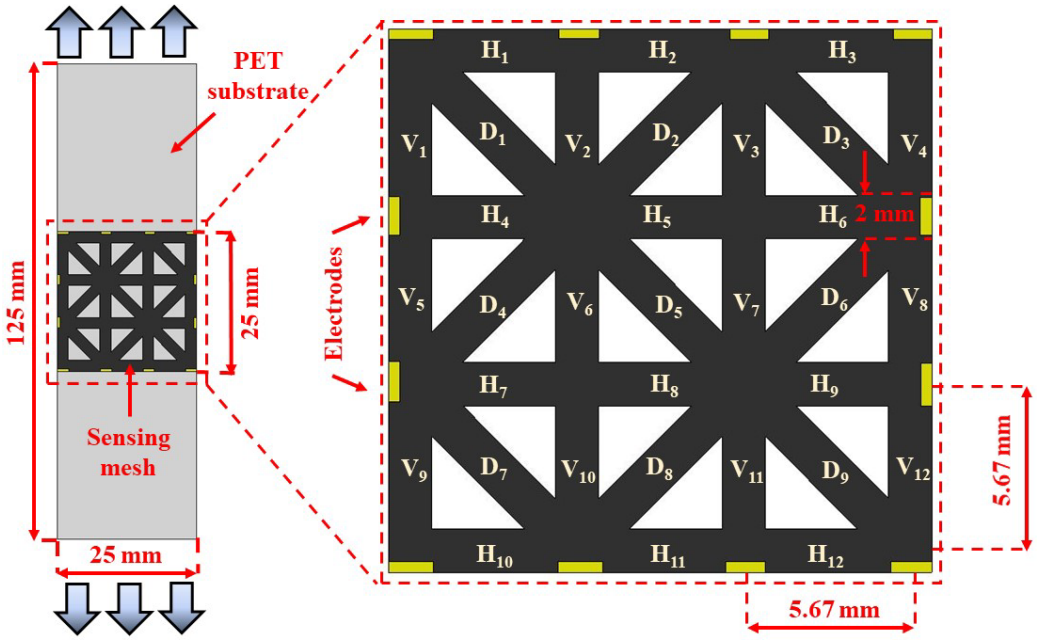

Figure 4. A grid-like sensing mesh was fabricated with diagonal struts and affixed onto a PET strip. The specimen was subjected uniaxial loading. H, V, and D indicate the horizontal, vertical, and diagonal struts, respectively.

conductivity distribution of the sensing mesh loaded to different strain states. The change in conductivity distributions of different strain states with respect to the baseline was then computed.

Second, a sensing mesh with diagonal struts was fabricated (Fig. 4), which followed the same fabrication process as discussed earlier. A total of 12 boundary electrodes were used. Instead of directly stretching the sensing mesh, it was affixed, using quick-curing superglue, at the center of a 125 × 25 mm^2 PET strip (Fig. 4). After the glue fully dried, the entire specimen was mounted in the Test Resource 150R load frame. A baseline EIT measurement was recorded when the specimen was unstrained (0 με). In contrast to the previous experiment, the test specimen was subjected to uniaxial tensile strain from 0 to 8,000 με in 2,000 με increments to allow for EIT testing. Here, loading rate was kept the same as previous tests (*i.e.*, 15,000 με/min).

Third, and following validation of the spatial strain sensing capabilities of the sensing mesh, a larger, 7 × 5 grid-like sensing mesh (Fig. 5a) was fabricated and affixed onto a poly(vinyl chloride) (PVC) plate (610-mm-long, 76.2-mm-wide, and 9.25-mm-thick) using quick-curing epoxy. A total of 16 EIT electrodes were attached to the boundaries of the sensing mesh. Because epoxy would infiltrate and affect the electrical and electromechanical properties of polymer-based nanocomposites, a Krylon acrylic coating was sprayed onto the sensing mesh to serve as a protective layer before it was attached to the PVC plate. For reference, a metal-foil strain gage (Tokyo Sokki Kenkyuio Co. Ltd. and gage factor = 2.13 ± 1%) was also mounted onto the PVC plate for measuring the induced strains in the longitudinal direction, as is illustrated in Fig. 5b.

After the epoxy was fully cured for ~ 6 h, the PVC plate, instrumented with the sensing mesh and strain gage, was mounted in an MTS-793 load frame. Like the previous experiments, a baseline EIT dataset was recorded prior to applying any load to the PVC plate. The load frame was programmed to apply monotonic uniaxial tensile loading to 10,000 με at a fixed strain rate of 1,000 με/min. The experimental setup is shown in Fig. 5c. The load frame was manually paused every 2,000 με, and the EIT DAQ interrogated the sensing mesh as described in Section III.C. In all these three sets of experiments, applied strains were calculated using the recorded grip displacements of the load frame in the vertical direction.

D. Damage Detection Validation

To further demonstrate its applicability for SHM, the sensing mesh was employed to detect damage and propagating cracks in an RC building subjected to shaking-table-induced earthquake excitations (Fig. 6a). The plan and isometric

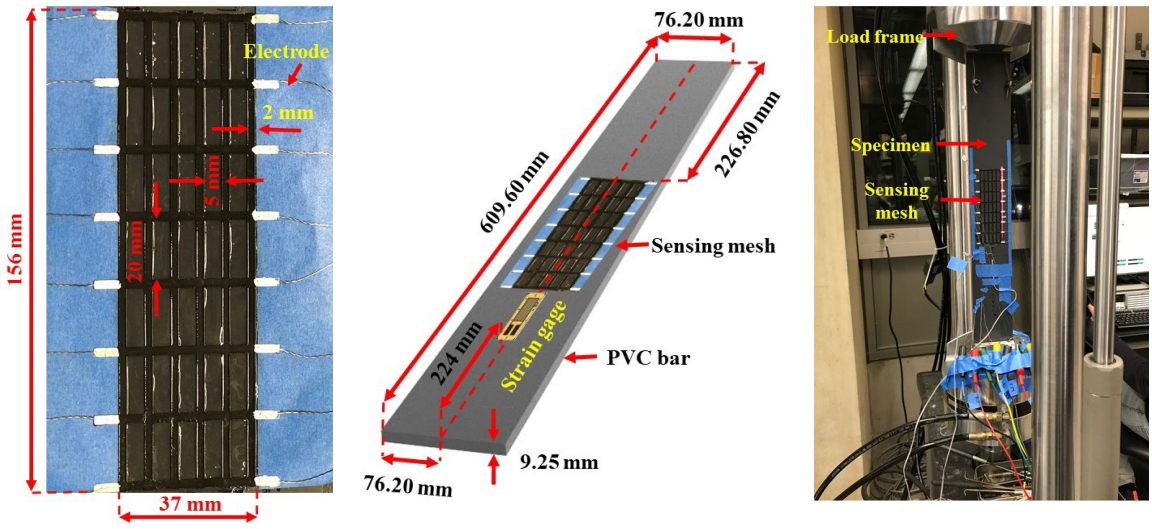

(a) (b) (c)

Figure 5. (a) A 7 × 5 sensing mesh was prepared and (b) epoxy-mounted onto a rectangular PVC plate. The PVC plate was also instrumented with a strain gage for measuring applied longitudinal strains. (c) The entire test specimen was mounted in a load frame and subjected to uniaxial tensile testing. The sensing mesh was interrogated at different strain states for EIT image reconstruction, while the strain gage simultaneously recorded the magnitude of induced strains in the plate.

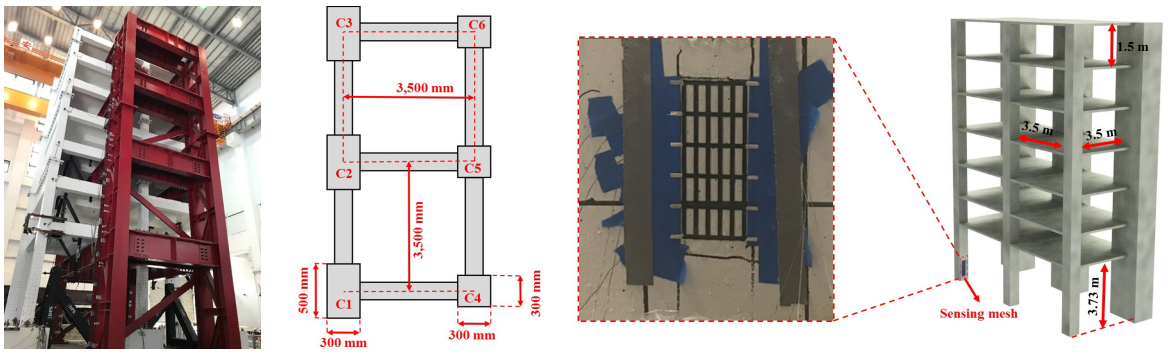

(a) (b) (c)

Figure 6. (a) A seven-story RC building was subjected to shaking table tests. (b) The plan view of the building and the dimensions of the structural components are shown. (c) The schematic of the entire test building is shown, where a 5 × 5 sensing mesh was affixed near the base of the left-most weak column (*i.e.*, C4).

views of the seven-story, two-bay, test structure are schematically shown in Figs. 6b and 6c, respectively. It can be seen from Fig. 6c that the height of the first floor (3.73 m) was greater than that of the other floors (1.5 m), which created a soft-story effect. In addition, the frame was designed such that the stiffnesses of columns C1, C2, and C3 were higher (due to their larger cross-sectional area) as compared to columns C4, C5, and C6 (Fig. 6b). The effect of this design means that the majority of damage would be concentrated in the first-floor.

Thus, a 5 × 5 sensing mesh was affixed near the base of column C4 (Fig. 6c) following the same mounting procedure discussed in Section III.C. For continuous and real-time data acquisition, a National Instruments (NI) PXIe-4302 system was customized with a PXIe-4139 source measuring unit (SMU), PXIe-4303 DAQ, and PXIe-2535 field-effect transistor (FET) switch. The SMU was used to supply the excitation current for EIT interrogation. As described in Section III.C, two adjacent electrodes were selected at a time, one for current injection and the other as ground, all controlled by a customized *LabVIEW* program. DC voltage measurements were continuously recorded at all analog

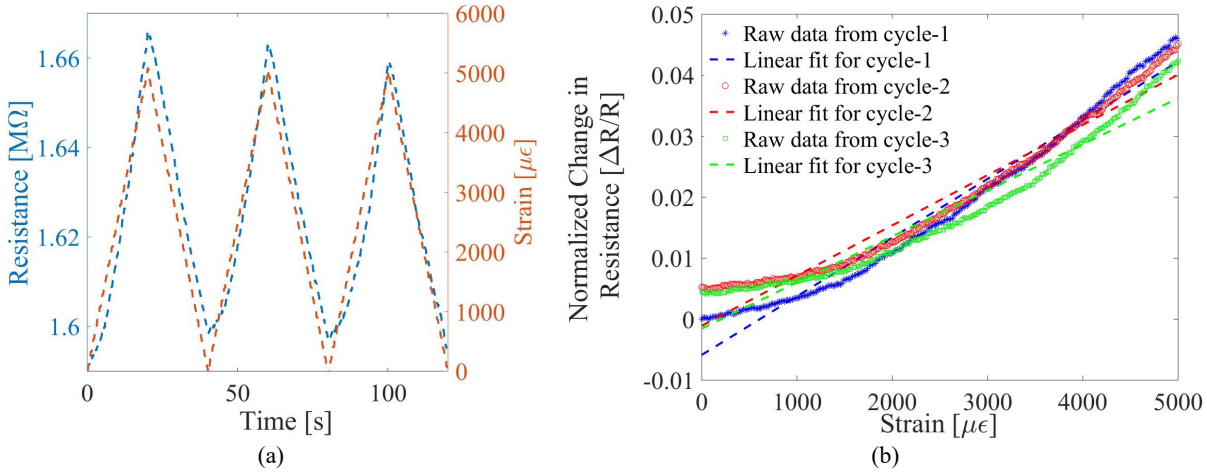

Figure 7. (a) The electrical resistance time history of a strained GNS-PVA thin film specimen is overlaid with the applied strain pattern. (b) Its normalized change in resistance over different loading cycles were computed and plotted with respect to of applied strains.

input (AI) channels of the PXIe-4303 DAQ. The effective sampling rate of the DAQ was such that EIT sensing mesh results could be acquired at 25 frames/s (or images/s).

The shaking table tests were conducted using a large-scale, high-performance shake table at the National Center for Research on Earthquake Engineering (NCREE) in Tainan, Taiwan. The entire structure was subjected to a sequence of dynamic loadings ranging from white-noise tests to different scaled earthquake ground motions of increasing intensity. The RC structure was tested until the weaker columns (*i.e.*, C5, C6, and C7) underwent catastrophic failure (*i.e.*, loss of load-carrying capacity).

IV. Results and Discussion

A. Strain Sensing Characterization

The strain sensing properties of the GNS-PVA thin films was characterized by conducting tensile cyclic tests, as was discussed in Section III.B. The thin films' resistance was measured throughout testing, as was the applied strains. A peak tensile strain of 5,000 με was applied to the specimens so that the films remained undamaged and linear-elastic.

Fig. 7a shows a representative GNS-PVA thin film's resistance response overlaid with the applied strain pattern. This result confirmed that the resistance of the thin film changed in tandem with applied strains. In addition, its electromechanical response was stable and repeatable. Furthermore, the same set of data was used to plot the normalized change in resistance versus strain as shown in Fig. 7b. Although Fig. 7b shows that the electromechanical performance of the GNS-PVA thin film was slightly nonlinear, a linear least-squares regression line was fitted to estimate their gage factor (G) or strain sensitivity (*i.e.*, the slope of the fitted line).

$$G = \frac{\Delta R / R_0}{\Delta \varepsilon} \tag{5}$$

where R_0 is the initial or unstrained resistance of the thin film, and ΔR is the change in resistance with respect to R_0 when strain ($\Delta\varepsilon$) is applied.

Fig. 8 plots the average G of each of the four specimens tested. The error bars in Fig. 8 indicate the standard deviations of G over different loading cycles. One can observe from the results that all of the four specimens exhibited comparable strain sensing properties, and the overall average gage factor was 8.20. Lee *et al.*[33] explained that high G of nanocomposite-based thin film strain sensors could be achieved if the concentration of nanomaterials were near or at the percolation threshold. As a result, minute tensile strains disrupt the electrically conductive pathways formed by the nanomaterials, thereby increasing strain sensitivity. As compared to the spray-fabricated CNT-based thin films

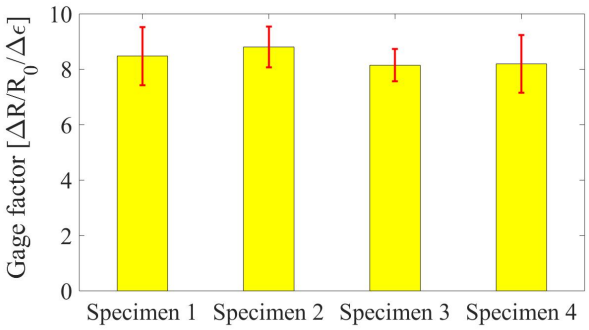

Figure 8. The average gage factors for four different thin film specimens tested are shown. The error bars indicate the standard deviations of the calculated gage factors over different loading cycles.

with a G of ~ 0.77 ± 0.02, which was reported by Mortensen *et al.*[34], the GNS-PVA thin films' were characterized by ~ 10 times higher G.

B. Sensing Mesh Verification

To demonstrate distributed strain field monitoring, GNS-PVA thin films were deposited onto PET grids to form sensing mesh specimens (Fig. 3a). EIT was used to determine the change in electrical conductivity of the sensing mesh corresponding to different strain states, and the results are shown in Fig. 9. It can be seen from Fig. 9 that the conductivity of the vertical thin film grid elements in the sensing mesh decreased (or resistivity increased) with greater applied tensile strains. These results were expected based on findings from Section IV.A. Furthermore, Fig. 9 also shows that the horizontal struts experienced an increase in conductivity, which is because of the induced compression due to stress concentrations at the junctions of the horizontal and vertical struts.

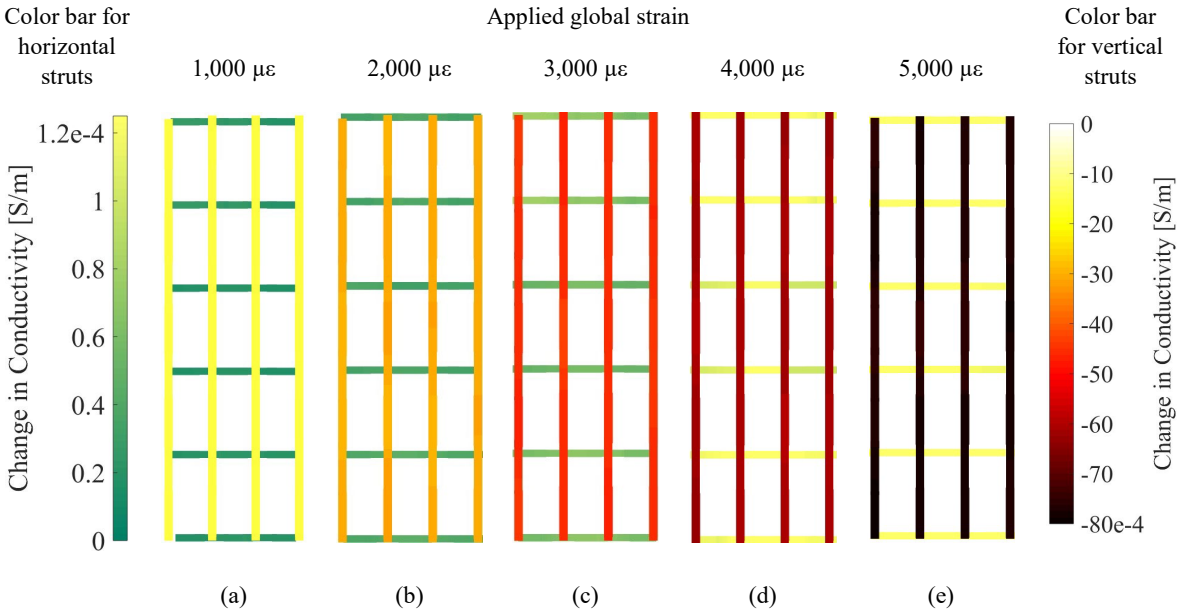

Figure 9. The sensing mesh was subjected to tensile strains, and the corresponding changes in electrical conductivity with respect to the undeformed state are shown in (a) to (e). Two separate color bars are used for visualizing conductivity changes for the horizontal (left) and vertical (right) struts, especially due to their different magnitudes of strains.

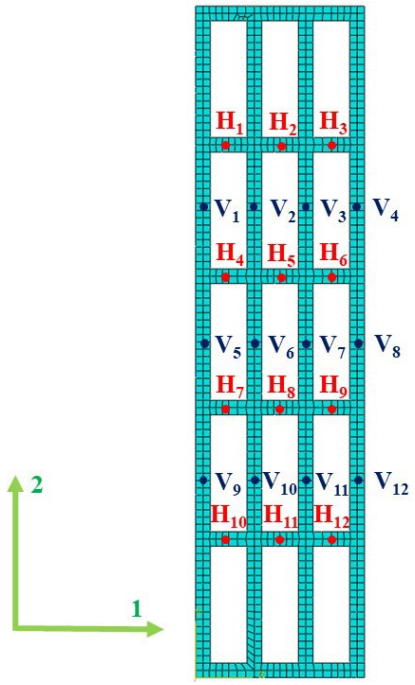

Figure 10. The discretized FE model of the sensing mesh is shown. $H_1 \ldots H_{12}$ and $V_1 \ldots V_{12}$ indicate midpoints of the corresponding horizontal and vertical struts, respectively.

To investigate the accuracy of the experimental EIT spatial strain sensing results, a linear-elastic finite element (FE) model of the sensing mesh was created in *ABAQUS*. PET was defined as having a Young's modulus and Poisson's ratio of 2 GPa and 0.44, respectively. The GNS-PVA film was not explicitly modeled, since its thickness and stiffness were negligible relative to PET. The entire model was discretized into 935 bi-linear quadrilateral elements as shown in Fig. 10. With the PET sensing mesh being only ~ 0.2-mm-thick and negligible compared to its other two dimensions (92 mm × 23 mm), plane stress was assumed. A pinned boundary condition was assigned for the bottom edge of the FE model, and tensile strain was applied at the top edge. The FE-estimated strain distributions (*i.e.*, ε_{11} and ε_{22}) corresponding to different applied global strain states are shown in Fig. 10. Similar to the experimental results (Fig. 9), ε_{22} (or strain in the vertical direction) increased with increasingly applied loads, while ε_{11} (or strain in the horizontal direction) was negative due to compression caused by Poisson's effect.

To compare the experimental EIT and FE simulation results, vertical (*i.e.*, $V_1 \ldots V_{12}$) and horizontal elements (*i.e.*, $H_1 \ldots H_{12}$) in the sensing mesh were identified according to Fig. 11. First, the EIT results were converted from conductivity distributions to strain maps. Here, the strains induced at the different elements in the struts ($\Delta\varepsilon$) were estimated by averaging the conductivity changes in all the finite elements of that particular strut ($\Delta\sigma$) and then normalizing with respect to the sensing mesh's initial conductivity (σ_o) (*i.e.*, unstrained conductivity) and G:

$$\Delta\varepsilon = \frac{\Delta\sigma / \sigma_0}{G} \tag{6}$$

In doing so, the EIT experimental results were directly comparable to the FE simulation strain maps. Second, the EIT-based strains corresponding to different struts when subjected to different global applied strains were compared against the FE model outputs (Fig. 12). Fig. 12 shows good agreement between the experimental and simulation results, where only an average of ~ 3% mismatch exists.

Three possible reasons could have contributed to these errors. First, misalignment and minor slippage of the sensing mesh from the load frame's grips during testing could have reduced the actual magnitude of applied strains. Second, the sensing meshes may have some slight inhomogeneities and nonuniform thickness due to fabrication error. Third, although it was assumed that the strains in the vertical members are uniform and equal to the applied global strains,

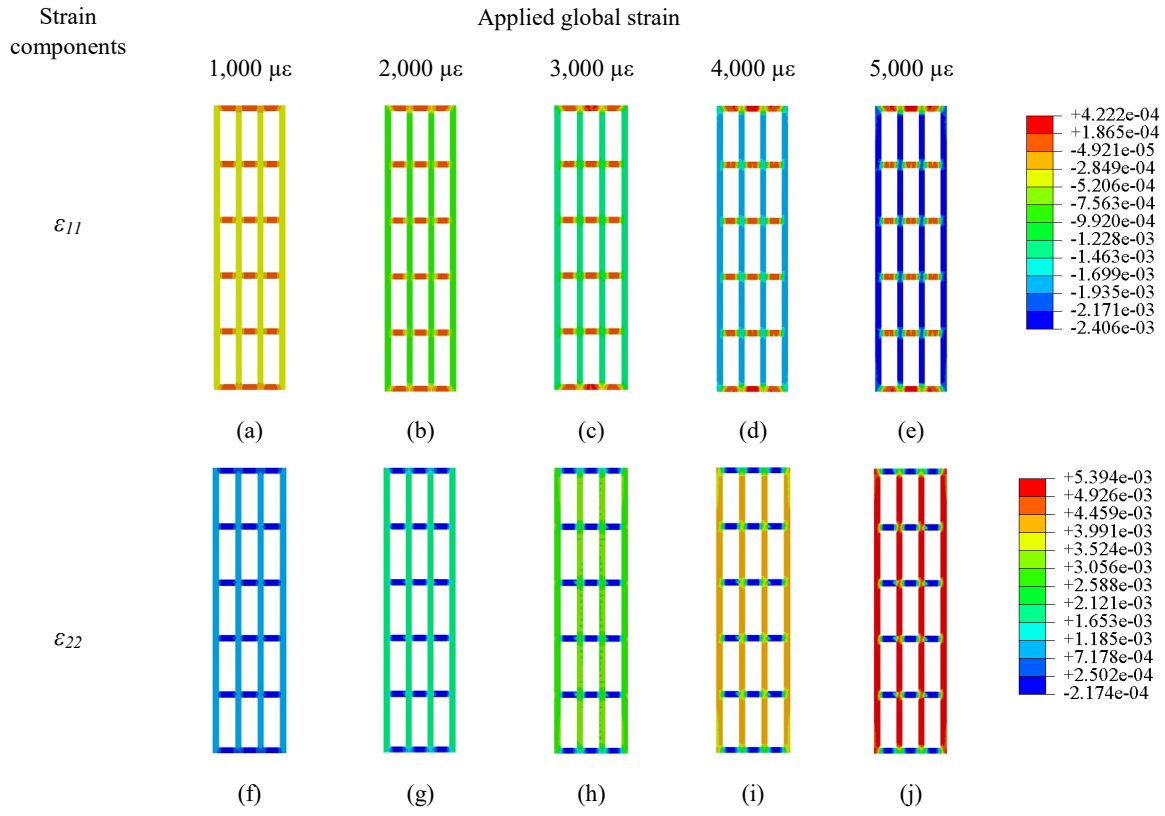

Figure 11. (a) to (e) and (f) to (j) show the distributions of ε_{11} and ε_{22}, respectively, over the entire sensing mesh when subjected to different tensile strains ranging from 0 to 5,000 με.

there may be stress concentrations close to the grips. The nonuniform strain distribution can be explained by Saint Venant's principle. In addition, the EIT results could have been affected by regularization incorporated as part of the inverse problem. Nevertheless, the 3% error was deemed acceptable.

Besides testing and loading the sensing mesh directly, a sensing mesh with diagonal struts was affixed onto a PET strip as shown in Fig. 4. Fig. 13 shows the reconstructed EIT conductivity maps of the sensing mesh corresponding to different applied global strain states. It can be observed that the conductivity of the vertical (*i.e.*, V_1, V_2,…,V_{12}) and diagonal struts (*i.e.*, D_1, D_2,…, D_9) decreased, while an opposite trend was observed for the horizontal members (*i.e.*, H_1, H_2, H_3,.., H_{12}). These results were expected, since the vertical and diagonal struts were subjected to tension, while the horizontal members experienced compression due to Poisson's effect. As a result, the magnitudes of induced strains in the horizontal members were ~ 42% of the tensile strains experienced by the vertical struts (Fig. 14).

Again, a similar plane stress FE model of the specimen was created in *ABAQUS* and discretized using 8,852 bi-linear quadrilateral elements. The same boundary condition was implemented (*i.e.*, pinned boundary condition) at one end of the PET strip. However, $\Delta\varepsilon$ was evaluated by estimating the change in their axial length (Δl) from the FE results and then dividing it by its original length (l_0), as is shown in (7):

$$\Delta\varepsilon = \frac{\Delta l}{l_0} \tag{7}$$

The EIT-estimated conductivity changes of all the finite elements in each strut were averaged and used to calculate the average induced strain in that strut using (6). The EIT-estimated strain of each strut was compared with the corresponding FE results and is shown in Fig. 14. Although good agreement between experimental and numerical results was found, a ~ 5% difference was observed. While Fig. 9 only demonstrated sensing strains in the horizontal and vertical directions, the results shown in Fig. 13 confirm the ability of the sensing mesh to measure strains along different directions.

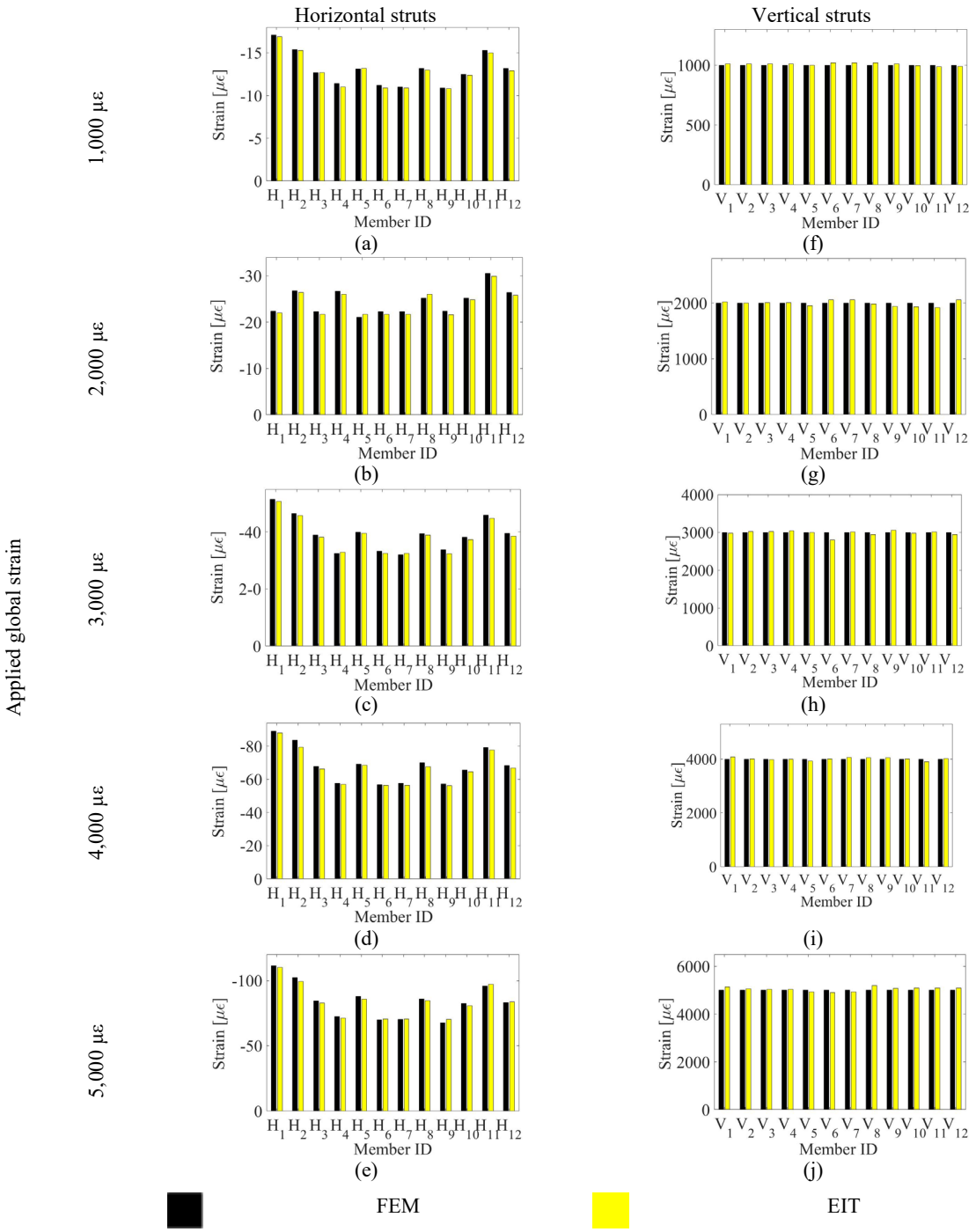

Figure 12. The FE and EIT test results for (a) to (e) the horizontal and (f) to (j) vertical struts corresponding to different applied strain states are compared.

C. Scaling Up the Sensing Mesh

A larger sensing mesh was also affixed onto PVC plates and loaded, as was described in Section III.D. Fig. 15 plots a set of EIT sensing mesh conductivity maps when the PVC plate was strained to 10,000 με. As expected, Fig. 15 clearly shows that the conductivity decreased in the vertical struts, while conductivity increased in all the horizontal struts. The magnitude of conductivity changes also increased as greater global tensile loading was applied to the PVC plate.

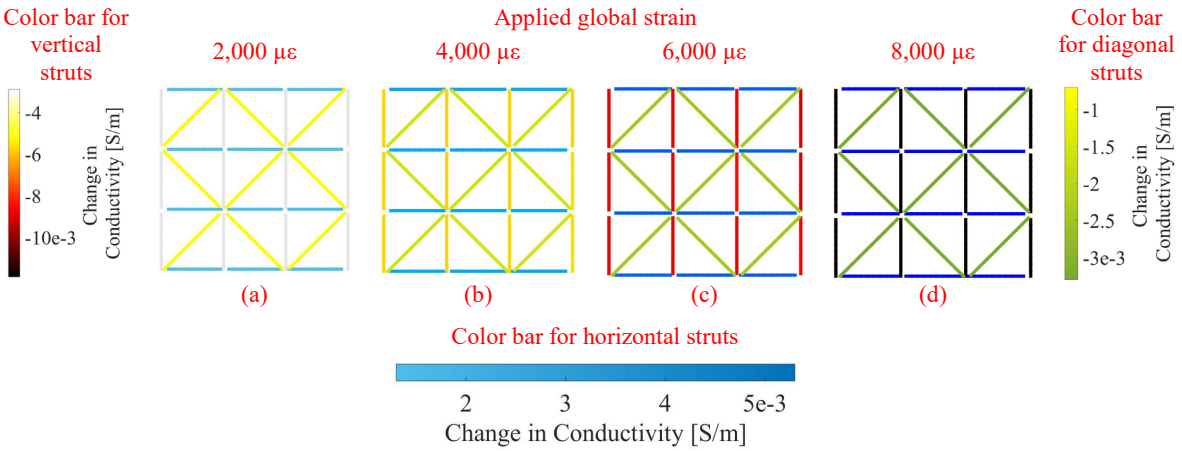

Figure 13. The average conductivity change of each strut with respect to their undeformed states (from EIT testing) are shown when the specimen was stretched to (a) 2,000, (b) 4,000, (c) 6,000, and (d) 8,000 με.

To further quantify the accuracy of these EIT sensing mesh results, they were compared to strain gage measurements of longitudinal strains in the PVC plate. Assuming strain was uniformly applied to the PVC plate, the resulting strains in all the vertical struts of the sensing mesh should be almost identical. Thus, the EIT strain measurements of the six vertical struts were directly compared with the strain gage readings in Fig. 16, where the results were found to be comparable with an average of ~ 4% error.

Some possible reasons for the errors observed could be due to imperfect strain transfer from the structural surfaces to the sensing meshes. In addition, the vertically applied tensile strains might not be uniformly distributed over the entire substrate, which again can be explained by Saint Venant's principle. Nevertheless, the results shown in Figs. 12 and 14 clearly show that the sensing mesh, when coupled with EIT, could effectively measure both the magnitude and directions of induced strains.

So far, the tests performed and the results obtained corresponded to situations when the structure was loaded and strained, and damage (*e.g.*, crack) was not present. If damage, such as a crack, occurs near the vicinity of the sensing mesh (but not directly underneath it), the local strain distribution underneath the sensing mesh will change due to the presence of the crack. In this scenario, the sensing meshes could capture the corresponding strain distribution of the structure but not necessarily identify the properties of the nearby crack. The next section examines the scenario when a crack in the structure propagates directly beneath the sensing mesh.

D. Damage Detection Validation

This study also investigated whether the sensing meshes could detect spatially distributed structural damage (*e.g.*, cracking) in a column of a seven-story RC building subjected to shaking table tests (Section III.E). EIT measurements were recorded continuously by the customized NI DAQ, while the building was subjected to near-fault earthquake excitations that caused severe damage in the structure. Fig. 17 plots three representative EIT sensing mesh results corresponding to before, during, and after shaking. First, it should be clarified that multiple shaking events were conducted during this test. However, the test results presented here only focused on one shaking event, specifically, when damage was induced at the location of the sensing mesh. Thus, previous shaking table events induced inelastic behavior in the structure and resulted in residual strains (and minor damage) in the column. The results shown in Fig. 17a show that the sensing mesh strain map was nonuniform because of this.

Second, Fig. 17b captured the sensing mesh strain distribution of the column when the structure (and column) was subjected to strong ground motions. It can be observed that localized changes in conductivity were observed in the second row of the sensing mesh. Finally, after shaking, Fig. 17c shows that the same vertical and horizontal struts exhibited a significant change in conductivity corresponding to the location of the crack that developed (Fig. 18). Thus, it was possible that Fig. 17b captured damage onset immediately prior to the crack opening to give the final results shown in Fig. 17c.

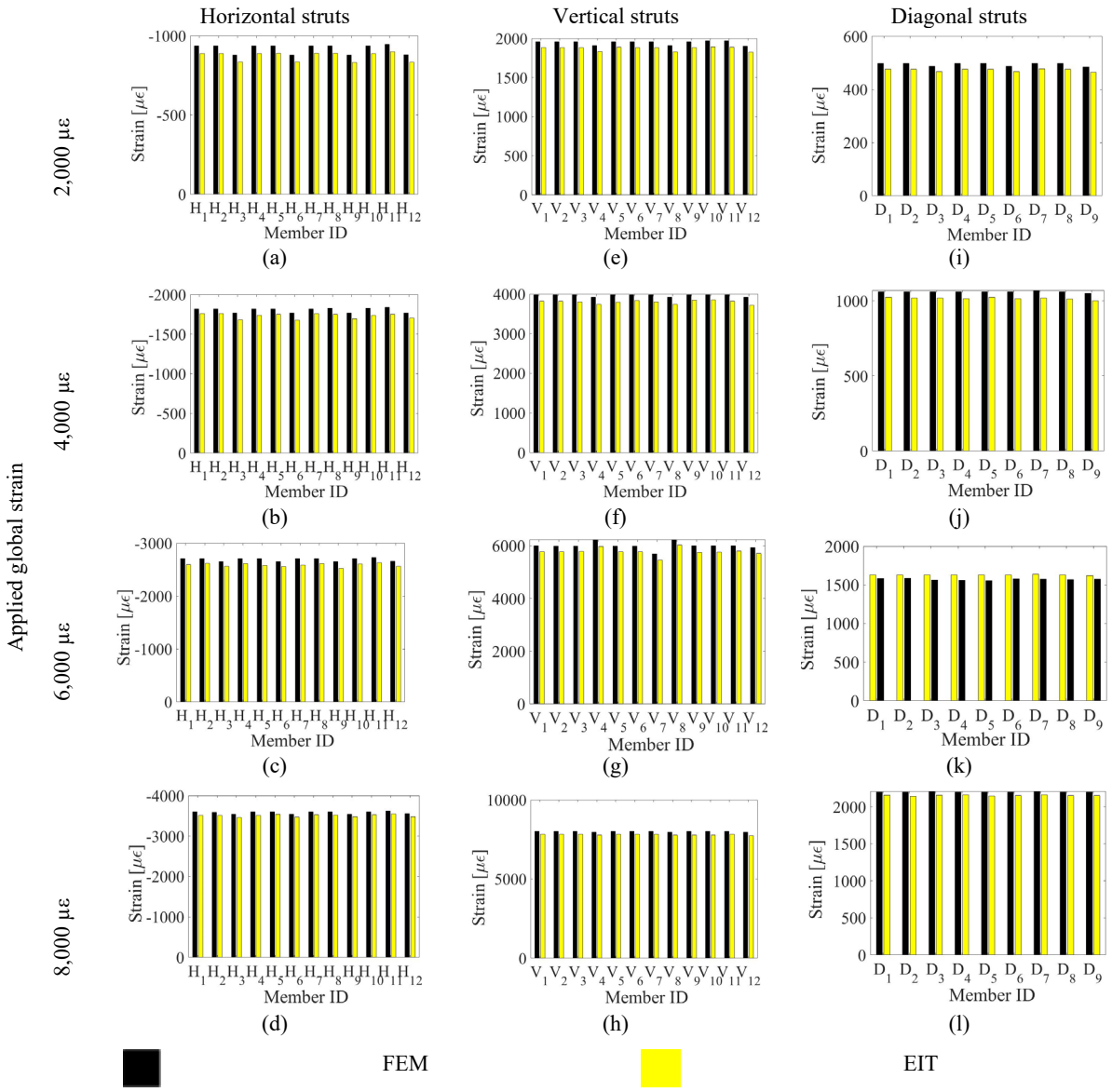

Figure 14. (a) to (d), (e) to (h), and (i) to (l) compare the EIT- and FE-estimated strains in the horizontal, vertical, and diagonal struts, respectively, when the specimen was subjected to different strain states.

Although crack propagation was successfully captured by the sensing mesh, conductivity changes in the other parts of the sensing mesh were observed in the reconstructed images. It was possible that, during shaking, the electrical cables connecting the sensing mesh were subjected to rigorous vibrations, thereby inducing more noise in the EIT boundary voltage measurements. Furthermore, unexpected changes in conductivity could have resulted from localized deformations of the column during shaking. Despite these, this preliminary large-scale test demonstrated the feasibility of using sensing meshes for crack damage detection and localization. Future research will focus on using sensing meshes for capturing dynamic structural response.

V. Significance of the Results

The significance of this study is the successful validation of distributed strain field monitoring using EIT coupled with a patterned nanocomposite sensing mesh. Previous work leveraged EIT for spatial sensing but was unable to resolve the different components of the strain tensor from reconstructed EIT conductivity maps. First, a new GNS-based

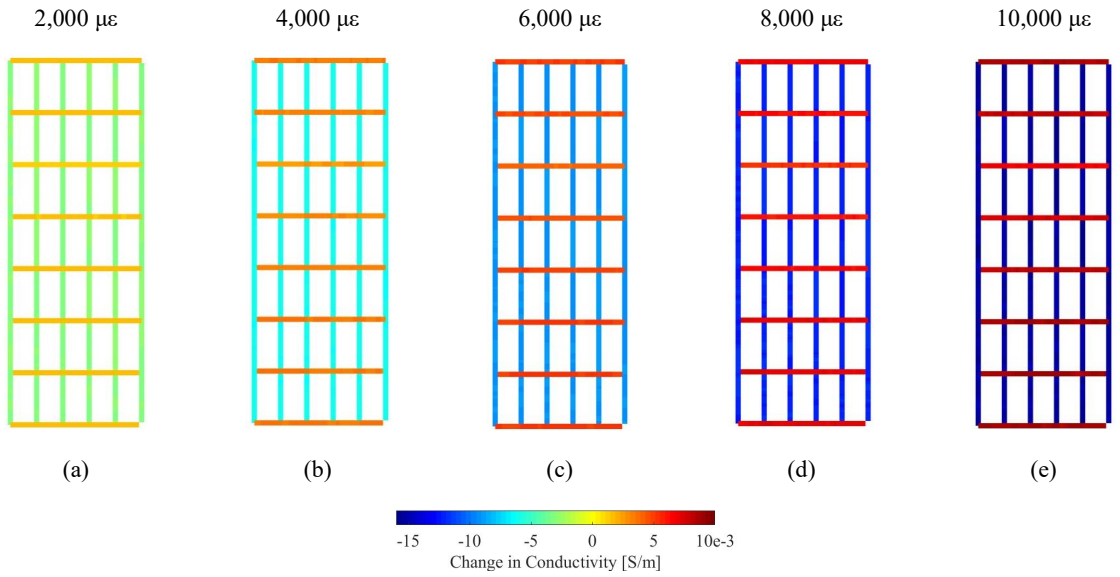

Figure 15. Tensile tests were performed on a PVC plate instrumented with a sensing mesh. EIT conductivity maps were obtained at (a) 2,000, (b) 4,000, (c) 6,000, (d) 8,000, and (e) 10,000 με. The changes in conductivity distributions with respect to the unstrained baseline are shown.

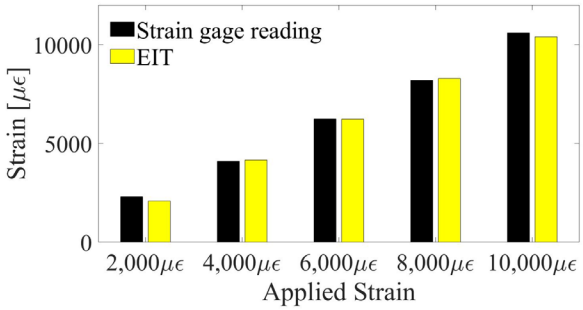

Figure 16. The EIT-based strain measurements are compared with strain gage readings of the PVC plate subjected to uniaxial tensile loading. Good agreement was observed.

nanocomposite whose electrical conductivity is sensitive to applied strains was also designed, fabricated, and characterized. Its strain sensitivity was found to be ~ 10 times higher than films used in other studies [10, 29, 34]. Second, in order to overcome this limitation, a patterned nanocomposite was proposed to replace conventional continuous thin films. Each strut of the sensing mesh was designed to be of a high aspect ratio to restrict sensing strain only along the longitudinal direction of each sensing mesh strut. Third, instead of employing 2D FEM for the EIT algorithm, each strut was discretized using uniaxial bar elements to capture the corresponding uniaxial behavior of the sensing mesh struts. This FEM implementation also significantly reduced the computational demand required to solve the EIT inverse problem, although this was not benchmarked against conventional EIT.

Last, the EIT-estimated strain field measurements from the experiments were compared with FEM results, and good agreement was observed. These findings added new knowledge to the field and offer a unique distributed sensing solution for SHM. The vision is that strain-sensitive nanocomposite-based sensing meshes will be deposited onto or embedded in large structures for *in situ* strain field monitoring.

VI. Conclusions

In this study, nanocomposite sensing meshes were designed for distributed strain field monitoring. Previous studies showed that piezoresistive thin films, when coupled with EIT, could monitor distributed strains and damage. However,

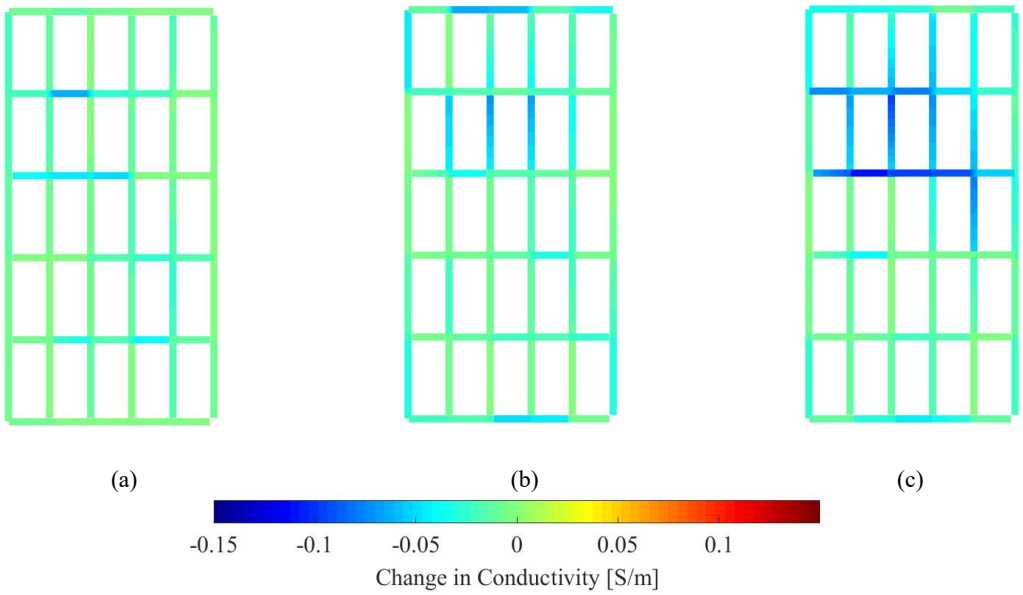

Figure 17. The changes in conductivity distributions of the sensing mesh with respect to the baseline (*i.e.*, before the building was subjected to shaking table earthquake excitations that generated a crack underneath the skin) were determined. EIT results (a) before, (b) during, and (c) after the earthquake ground motion excitation test are shown.

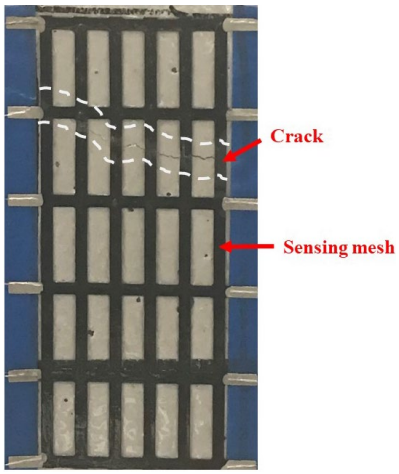

Figure 18. A transverse crack developed underneath the sensing mesh (near its second row) after the test structure was subjected to strong ground shaking.

the low strain sensitivity of the thin film and the inability of EIT to resolve the directionality of strain components were two barriers for field deployment. To overcome these challenges, highly strain-sensitive GNS-PVA thin films were designed and fabricated by spray coating. The characterization study revealed that the gage factor of the thin film strain sensor was more than 10 times higher than previous carbon nanotube-based films. Then, sensing meshes were fabricated by spray coating GNS-PVA thin films onto grid-like PET cutouts. An updated EIT algorithm was also implemented to more efficiently capture changes in sensing mesh conductivities.

The test results showed that EIT was able to identify if any of the struts aligned at different directions in the sensing mesh was subjected to tension or compression (*i.e.*, in their respective orientations). These experimental EIT results were compared with FE analysis for verification, and good agreement was observed. A larger-scale sensing mesh was also employed for monitoring strain distributions in a PVC plate subjected to uniaxial tensile loading. The EIT-derived

strain measurements that were compared with strain gage readings showed good agreement. Last, for validation, the sensing mesh was utilized for damage detection in a column of a seven-story RC building subjected to earthquake excitations. The reconstructed spatial conductivity maps showed localized decreases in conductivity corresponding to locations where a crack propagated. Overall, the results successfully validated sensing meshes for strain field monitoring and spatial damage detection.

Although the GNS-PVA thin film had high strain sensitivity and could be scaled up through the use of spray fabrication, the high electrical resistance of the polymer matrix (*i.e.*, PVA) can pose a challenge for large-scale applications. Since EIT requires propagating electrical current through the entire sensing mesh, the electrical resistance of the film should be managed accordingly. Future work will consider alternative polymer matrices or additional additives for tuning the overall resistivity (or conductivity) of the films. In addition, the thin film's sensitivity can also be further improved to enhance sensing resolution.

Acknowledgements

This research was supported by the U.S. Army Corp of Engineers under Research Cooperative Agreement W912HZ-17-2-0024, and partial support was also provided by the Jacobs School of Engineering, University of California-San Diego. The authors gratefully acknowledge the National Center for Research on Earthquake Engineering in Tainan, Taiwan for giving us access and allowing our participation in the shaking table tests. The authors also thank Prof. Hyonny Kim (Department of Structural Engineering, University of California-San Diego) for providing access to the MTS-793 load frame and Mr. Konstantinos Anagnostopoulos for his help with load testing. This study was also conducted in collaboration with Prof. Michael D. Todd (University of California-San Diego), Dr. A. Drew Barnett and Dr. Joey Reed (Elintrix), and Dr. Anton Netchaev (Engineering Research & Development Center, U.S. Army Corp of Engineers).

Author Contributions

S. Gupta developed the GNS thin film and implemented the EIT algorithm. He planned the experimental tests and analyzed the results with the help and supervision of K. J. Loh. W. H. Chiang synthesized the GNS used in this study. S. Gupta and G. Vella conducted the experiments together. K. J. Loh collaborated with C-H. Loh and instrumented the sensing mesh in the large-scale test building that was subjected to shaking table tests in Taiwan. I. Yu assisted S. Gupta, G. Vella, and K. J. Loh to install the sensing mesh on the RC building and coordinated the large-scale tests. S. Gupta and K. J. Loh wrote the manuscript. K. J. Loh is the principal investigator of this project (supported by the U.S. Army Corp of Engineers) and supervised the entire study.

Competing Interests

The authors declare no conflicts of interest.

References

1. Farrar, C. R., and Worden, K. An Introduction to Structural Health Monitoring. Philosophical Transactions: Mathematical, Physical and Engineering Sciences. 2007; 365(1851):303-15.
2. Kersey, A. D., Davis, M. A., Patrick, H. J., Koo, M. L., Askins, C. G., Putnam, M. A., and Friebele, E. J. Fiber Grating Sensors. Journal of Lightwave Technology 1997; 15(8):1442-63.
3. Li, H. N., Li, D. S., and Song, G. B. Recent Applications of Fiber Optic Sensors to Health Monitoring in Civil Engineering. Engineering Structures. 2004; 26(11):1647-57.
4. Glišić, B., Yao, Y., Tung S, T., Wagner, S., Sturm J, C., and Verma, N. Strain Sensing Sheets for Structural Health Monitoring Based on Large-Area Electronics and Integrated Circuits. Proceedings of the IEEE. 2016; 104(8):1513-28.
5. Kharroub, S., Laflamme, S., Song, C., Qiao, D., Phares, B., and Li, J. Smart Sensing Skin for Detection and Localization of Fatigue Cracks. Smart Materials and Structures. 2015; 24(6):1-16.
6. Dharap, P., Li, Z., Nagarajaiah, S., and Barrera E, V. Nanotube Film Based on Single-Wall Carbon Nanotubes for Strain Sensing. Nanotechnology. 2004; 15(3):379-82.
7. Loh, K. J., Kim, J., Lynch, J. P., Kam, N. W., and Kotov, N. A. Multifunctional Layer-by-Layer Carbon Nanotube–Polyelectrolyte Thin Films for Strain and Corrosion Sensing. Smart Materials and Structures. 2007; 16(2):429-38.
8. Hou, T. C., Loh, K. J., and Lynch, J. P. Spatial Conductivity Mapping of Carbon Nanotube Composite Thin Films by Electrical Impedance Tomography for Sensing Applications. Nanotechnology. 2007; 18(31):315501.
9. Loh, K. J., Hou, T. C., Lynch, J. P., and Kotov, N. A. Carbon Nanotube Sensing Skins for Spatial Strain and Impact Damage Identification. Journal of Nondestructuctive Evaluation. 2009; 28(1):9-25.

10. Loyola, B. R., Saponara, V. L., Loh, K. J., Briggs, T. M., G. O'Bryan, and Skinner, J. L. Spatial Sensing Using Electrical Impedance Tomography. IEEE Sensors (1530-437X). 2013; 13(6):2357-67.
11. Hallaji, M., Seppänen, A., and Pour-Ghaz, M. Electrical Impedance Tomography-Based Sensing Skin for Quantitative Imaging of Damage in Concrete. Smart Materials and Structures. 2014; 23(8):085001.
12. Gupta, S., Gonzalez, J. G., and Loh, K. J. Self-Sensing Concrete Enabled by Nano-Engineered Cement-Aggregate Interfaces. Struct Health Monit. 2016; 16(3):309-23.
13. Tallman, T. N., Gungor, S., Koo, G. M., and Bakis, C. E. On the Inverse Determination of Stresses and Strains in a Carbon Nanofiber/Polyurethane Nanocomposite from Conductivity Data Obtained Via Electrical Impedance Tomography. Journal of Intelligent Material Systems and Structures. 2017; 28:2617-29.
14. Soleimani, M. Image and Shape Reconstruction Methods in Magnetic Induction and Electrical Impedance Tomography. Ph.D. Thesis. Manchester, England: University of Manchester; 2005.
15. Vauhkonen, M. Electric Resistance Tomography and Prior Information. Ph.D. Thesis. Kuopio, Finland: University of Kuopio; 1997.
16. Barber, D. Quantification in Impedance Imaging. Clinical Physics and Physiological Measurement. 1990 11(4A):45-56.
17. Dijkstra, A. M., Brown, B. H., Leathard, A. D., Harris, N. D., Barber, D. C., and Edbrooke, D. L. Review Clinical Applications of Electrical Impedance Tomography. Journal of Medical Engineering & Technology. 1990; 17(3):89-98.
18. Murphy, D. B., Coombs, P., Tarassenko, L., and Rolfe, P. Impedance Imaging in the Newborn. Clinical Physics and Physiological Measurement. 1987; 8(4A):131-40.
19. Newell, J. C., Edic, P. M., Ren, X., Larson-Wiseman, J. L., and Danyleiko, M. D. Assessment of Acute Pulmonary Edema in Dogs by Electrical Impedance Imaging. IEEE Transactions on Biomedical Engieering. 1996.
20. Smallwood, R. H., Mangnall, Y. F., and Leathard, A. D. Transport of Gastric Contents (Electric Impedance Imaging). Physiological Measurement. 1994; 15(2A):A175.
21. Loh, K. J., and Azhari, F. Recent Advances in Skin-Inspired Sensors Enabled by Nanotechnology. Journal of Materials (1047-4838). 2012; 64(7):793-801.
22. Hanke, M., Harrach, H., and Hyvönen, N. Justification of Point Electrode Models in Electrical Impedance Tomography. Mathematical Models and Methods in Applied Sciences. 2011; 21(06):1395-413.
23. Yang, L., Mohammed, A., Mohamadou, Y., Oh, T. I., and Soleimani, M. Complex Conductivity Reconstruction in Multiple Frequency Electrical Impedance Tomography for Fabric-Based Pressure Sensor. Sensor Review. 2015; 35(1):85-97.
24. Yorkey, J., Webster, J. G., and Tompkins, W. J. Comparing Reconstruction Algorithms for Electrical Impedance Tomography. IEEE Transactions on Biomedical Engineering. 1987; 34(11):843-52.
25. Chen, X., Zheng, X., Kim, J. K., Li, X., and Lee, D. W. Investigation of Graphene Piezoresistors for Use as Strain Gauge Sensors. Journal of Vacuum Science & Technology B, Nanotechnology and Microelectronics: Materials, Processing, Measurement, and Phenomena. 2011; 29(6):06FE1.
26. Bae, S. H., Lee, Y., Sharma, B. K., Lee, H. J., Kim, J. H., and Ahn, J. H. Graphene-Based Transparent Strain Sensor. Carbon. 2013; 51:236-42.
27. Liu, Q., Chen, J., Li, Y., and Shi, G. High-Performance Strain Sensors with Fish-Scale-Like Graphene-Sensing Layers for Full-Range Detection of Human Motions. ACS Nano. 2016; 10(8):7901-6.
28. Tian, H., Shu, Y., Cui, Y., Mi, W., Yang, Y., Xie, D., and Ren, T. Scalable Fabrication of High-Performance and Flexible Graphene Strain Sensors. Nanoscale. 2013; 6:699-705.
29. Wang, L., Loh, K. J., Chiang, W.-H., and Manna, K. Micro-Patterned Graphene Sensing Skins for Human Physiological Monitoring. Nanotechnology (0957-4484). 2018; 29(10):105503.
30. Manna, K., Hsieh, C. Y., Lo, S. C., Li, Y. S., Huang, H. N., and Chiang, W. H. Graphene and Graphene-Analogue Nanosheets Produced by Efficient Water-Assisted Liquid Exfoliation of Layered Materials. Carbon. 2016; 105:551-5.
31. Manna, K., Huang, H. N., Li, W. T., Ho, Y. H., and Chiang, W. H. Toward Understanding the Efficient Exfoliation of Layered Materials by Water-Assisted Cosolvent Liquid-Phase Exfoliation. Chemistry of Materials. 2016; 28(21):7568-93.
32. Hilding, J., Grulke, E. A., Zhang, G., and Lockwood, F. Dispersion of Carbon Nanotubes in Liquids. Journal of Dispersion Science and Technology. 2003; 24(1):1-41.
33. Lee, B. M., and Loh, K. J. Carbon Nanotube Thin Film Strain Sensors: Comparison between Experimental Tests and Numerical Simulations. Nanotechnology. 2017; 28:155502.
34. Mortensen, L. P., Ryu, D., Zhao, Y., and Loh, K. J. Rapid Assembly of Multifunctional Thin Film Sensors for Wind Turbine Blade Monitoring. Key Engineering Materials Journal (1013-9826). 2013; 569-570:515-22.